JACS
JOURNAL OF THE AMERICAN CHEMICAL SOCIETY
Article
pubs.acs.org/JACS

Ag−Sn Bimetallic Catalyst with a Core−Shell Structure for CO_2 Reduction

Wesley Luc,[†] Charles Collins,[†] Siwen Wang,[‡] Hongliang Xin,[‡] Kai He,[§,∥] Yijin Kang,[§,⊥] and Feng Jiao*[,†]

[†]Center of Catalytic Science and Technology, Department and Biomolecular Engineering, University of Delaware, Newark, Delaware 19716, United States

[‡]Department of Chemical Engineering, Virginia Polytechnic Institute and State University, Blacksburg, Virginia 24061, United States

[§]Department of Materials Science and Engineering, Northwestern University, Evanston, Illinois 60208, United States

[∥]NUANCE Center, Northwestern University, Evanston, Illinois 60208, United States

[⊥]Institute of Fundamental and Frontier Sciences, University of Electronic Science and Technology of China, Chengdu, Sichuan 610054, PR China

Supporting Information

ABSTRACT: Converting greenhouse gas carbon dioxide (CO_2) to value-added chemicals is an appealing approach to tackle CO_2 emission challenges. The chemical transformation of CO_2 requires suitable catalysts that can lower the activation energy barrier, thus minimizing the energy penalty associated with the CO_2 reduction reaction. First-row transition metals are potential candidates as catalysts for electrochemical CO_2 reduction; however, their high oxygen affinity makes them easy to be oxidized, which could, in turn, strongly affect the catalytic properties of metal-based catalysts. In this work, we propose a strategy to synthesize Ag−Sn electrocatalysts with a core−shell nanostructure that contains a bimetallic core responsible for high electronic conductivity and an ultrathin partially oxidized shell for catalytic CO_2 conversion. This concept was demonstrated by a series of Ag−Sn bimetallic electrocatalysts. At an optimal SnO_x shell thickness of ∼1.7 nm, the catalyst exhibited a high formate Faradaic efficiency of ∼80% and a formate partial current density of ∼16 mA cm^{-2} at −0.8 V vs RHE, a remarkable performance in comparison to state-of-the-art formate-selective CO_2 reduction catalysts. Density-functional theory calculations showed that oxygen vacancies on the SnO (101) surface are stable at highly negative potentials and crucial for CO_2 activation. In addition, the adsorption energy of CO_2^- at these oxygen-vacant sites can be used as the descriptor for catalytic performance because of its linear correlation to OCHO* and COOH*, two critical intermediates for the HCOOH and CO formation pathways, respectively. The volcano-like relationship between catalytic activity toward formate as a function of the bulk Sn concentration arises from the competing effects of favorable stabilization of OCHO* by lattice expansion and the electron conductivity loss due to the increased thickness of the SnO_x layer.

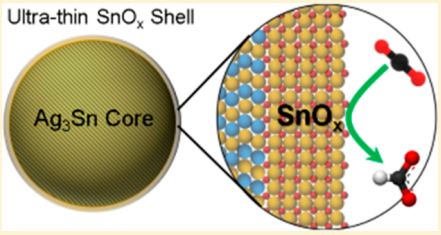

INTRODUCTION

An attractive strategy of combating rising atmospheric CO_2 emissions is to use renewable energy to power the electrochemical conversion of CO_2, captured from chemical plants, into value-added carbon-based products.[1−7] This will provide a 2-fold benefit of reducing CO_2 emission while providing an economically viable pathway for renewable energy storage and utilization. However, CO_2 is a fully oxidized and thermodynamically stable molecule, and therefore, suitable catalysts are needed to facilitate the chemical transformation of CO_2 in order to minimize the energy penalty associated with the CO_2 reduction reaction. The most widely studied CO_2 reduction electrocatalysts are precious metals, such as Au and Ag, because they have high electrical conductivity, good activity and stability under reaction conditions.[8−12] Nonprecious metals such as Cu, Sn, and Zn have also shown interesting properties in CO_2 electrolysis.[13−18] However, the oxophilic nature of those metals makes it extremely difficult to control surface structures, in sharp contrast with precious metals. Furthermore, the majority of metal oxides are poorly conductive; and thus, bulk metal oxides are not attractive catalysts for CO_2 electroreduction. In the case of nanosized nonprecious catalysts, the control of surface properties becomes even more challenging because of their high surface areas in comparison to their bulk counterparts. Therefore, regardless of the morphology, metal oxides are rarely considered as efficient CO_2 electrocatalysts.[19]

Recently, Gao et al. reported that a partially oxidized cobalt catalyst with a two-dimensional (2D) layered structure was able to reduce CO_2 electrochemically to formate at low overpotentials.[20] Different from bulk cobalt oxides that are inactive for CO_2 reduction, the cobalt layered catalyst with a thickness of ∼0.84 nm exhibited a superior and stable electrocatalytic performance. This distinctive catalytic property is likely due to

Received: October 7, 2016
Published: January 17, 2017

DOI: 10.1021/jacs.6b10435
J. Am. Chem. Soc. 2017, 139, 1885−1893

the extremely thin 2D structure that ensured good electrical conductivity as well as a good contact between the catalyst and the conductive substrate. While the 2D cobalt layered catalyst showed interesting electrocatalytic properties, the low surface area nature of the electrode resulted in relatively low formate partial current density (~8 mA cm^{-2}). Moreover, 2D layered catalysts are also difficult to process with commonly used three-dimensional (3D) porous substrates such as carbon paper in order to create high surface area electrodes. In contrast, nanoparticulate catalysts are relatively easier to process; however, their oxide form is not active for CO_2 electroreduction.

One potential solution to address this issue is to design a core−shell nanoparticle catalyst with a metallic core that ensures high electrical conductivity and a thin shell, either metallic or partially oxidized, that can be tailored for high electrocatalytic activity. Here, we demonstrate this concept with a model core−shell electrocatalyst that has a Ag−Sn bimetallic core and an ultrathin partially oxidized SnO_x shell (denoted as AgSn/SnO_x) for CO_2 reduction to formate with high Faradaic efficiencies and high current densities. A structure−activity correlation between the AgSn/SnO_x core−shell structure and CO_2 electrocatalytic activity was established by studying a series of Ag−Sn catalysts with different Ag/Sn compositions. More importantly, a volcano-like correlation between the bulk composition and electrocatalytic performance was observed, in which the optimal thickness of the partially oxidized SnO_x shell was ~1.7 nm. Density-functional theory calculations suggested that the SnO with oxygen vacancies is the active phase for CO_2 reduction at highly negative potentials and CO_2 adsorption energy at these vacant sites can be used as the reactivity descriptor for catalytic performance. As the Sn concentration increased in the Ag−Sn core, the OCHO* intermediate for the HCOOH formation pathway was further stabilized compared to the COOH* intermediate that is responsible for CO production, thus enhancing the Faradaic efficiency toward HCOOH. The decrease in current density for catalysts with high Sn concentrations was due to the increased thickness of oxide layer.

RESULTS

Synthesis and Structural Characterization. The synthesis of AgSn/SnO_x core−shell catalysts began with the formation of metallic Sn seeds in the presence of polyvinylpyrrolidone (PVP), followed by galvanically displacing Sn with Ag.[21] A schematic diagram representing the synthetic approach is shown in Scheme 1. To access AgSn/SnO_x catalysts with different compositions, the molar ratio of Sn and Ag precursors was tuned accordingly. The compositions of the resulting catalysts were determined by the Wavelength Dispersive X-ray Fluorescence (WDXRF) analysis and the results (Supplementary Table S1) confirmed that the actual compositions closely matched the expected values.

Scheme 1. Synthesis of Ultrathin Partially Oxidized Tin Oxide Catalyst for CO_2 Electroreduction

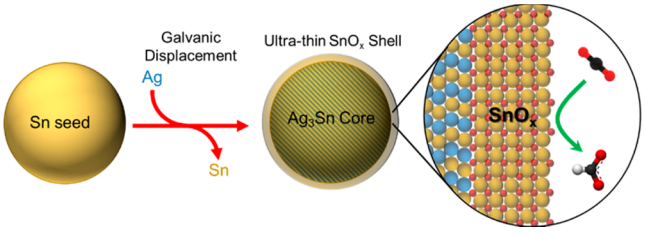

The morphology of as-synthesized AgSn/SnO_x catalysts was characterized by scanning electron microscopy (SEM). Figure 1a shows a typical SEM image of $Ag_{76}Sn_{24}$, in which finely dispersed nanoparticles with a particle size of ~20 nm and a near-spherical shape are evident. The particle size and distribution are similar to those of other Ag/Sn compositions (Supplementary Table S1 and Supplementary Figure S1). Transmission electron microscopy (TEM) was used to examine the structure of the AgSn/SnO_x catalysts. The TEM image of $Ag_{76}Sn_{24}$ (Figure 1b) shows near-spherical particles with a size of ~20 nm, which is in good agreement with the SEM results (Supplementary Table S1). A close examination of the as-synthesized $Ag_{76}Sn_{24}$ catalyst using high-resolution TEM (HRTEM) confirmed that the catalyst particles had a core−shell structure (Figure 1c). The shell was highly disordered (i.e., amorphous) with a thickness of approximately 1.7 nm, while the core appeared to be highly ordered (i.e., crystalline). The distance between two neighboring crystal lattice fringes was 0.259 nm, which corresponded to the interplanar spacing of Ag_3Sn (110) planes (Figure 1c). The HRTEM results suggest that the core was crystalline Ag_3Sn and the shell was an amorphous metal oxide layer with a thickness less than 2 nm.

To examine the core−shell structure in detail, high-angle annular dark-field scanning TEM (HAADF-STEM) imaging and electron energy-loss spectroscopy (EELS) were performed on the $Ag_{76}Sn_{24}$ catalyst. Figures 1d−h exhibit the STEM-EELS chemical maps acquired over the region shown within the green box in Figure 2d by exploiting the background-subtracted characteristic EELS edges of Sn-$M_{4,5}$ (485 eV), Ag-$M_{4,5}$ (367 eV), and O−K (532 eV), respectively. Figures 1g and 1h indicate that majority of the O species were confined to the surface, while the Sn and Ag elements were distributed throughout the particle. From line-point position analysis, Sn was mostly uniform throughout the particle with Ag being randomly distributed (Supplementary Figure S2). The results strongly suggest that the O species were likely associated with the amorphous SnO_x shell, which was also observed in the HRTEM analysis (Figure 1c). Additional EELS results for other compositions can be found in the Supplementary Figure S3.

The partially oxidized SnO_x shell was also confirmed by X-ray photoelectron spectroscopy (XPS) analysis. Figure 2 shows the $Ag_{76}Sn_{24}$ survey spectrum and typical XPS fittings of O 1s, Ag 3d, and Sn 3d spectra. The adventitious carbon peak was calibrated to 285.0 eV. The XPS spectra showed the presences of O^{2-} (530.2 eV), $Sn^{2+/4+}$ (486.9 and 495.3 eV), Sn^0 (485.1 and 493.5 eV), and Ag^0 (368.1 and 374.1 eV) on the catalyst surface. Because there was no oxidized silver detected on the surface by XPS, the amorphous oxide layer identified by TEM studies was most likely associated with a thin layer of partially oxidized SnO_x. On the basis of all the structural characterization results, we concluded that the $Ag_{76}Sn_{24}$ catalyst was composed of ~20 nm near-spherical nanoparticles with a core−shell structure, where the core was crystalline Ag_3Sn and the shell was a ~1.7 nm amorphous SnO_x layer. The AgSn/SnO_x catalysts with other compositions were also investigated using XPS and the surface compositions are summarized in the Supplementary Table S2. As the bulk Sn concentration in the AgSn/SnO_x catalysts increased, the amount of oxidized tin species (i.e., Sn^{2+} and/or Sn^{4+}) on the surface increased, while the amount of metallic Ag decreased. The surface compositions

DOI: 10.1021/jacs.6b10435
J. Am. Chem. Soc. 2017, 139, 1885−1893

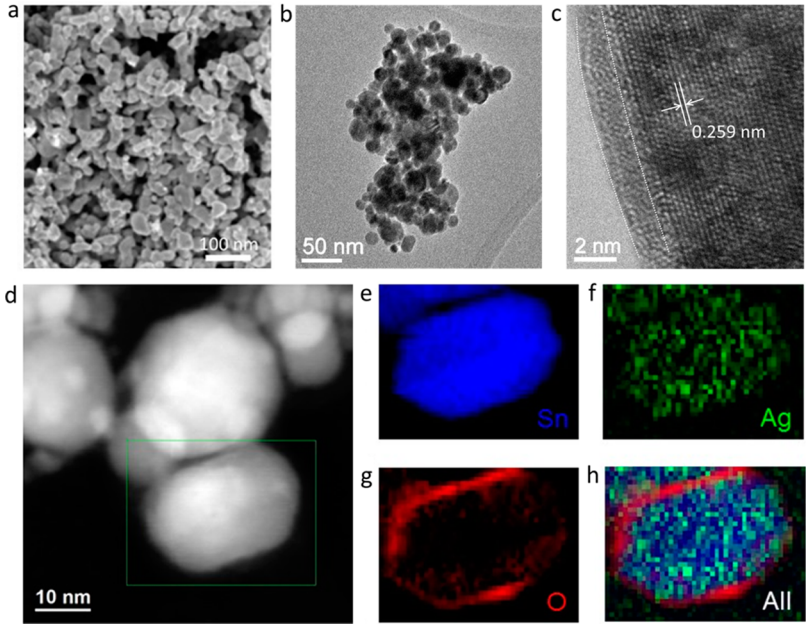

Figure 1. (a) SEM image of $Ag_{76}Sn_{24}$, (b, c) TEM images of $Ag_{76}Sn_{24}$, (d) HAADF-STEM image of $Ag_{76}Sn_{24}$, (e–h) EELS mapping of the selected region showing elemental distribution of Sn (e), Ag (f), O (g) and their overlay (h).

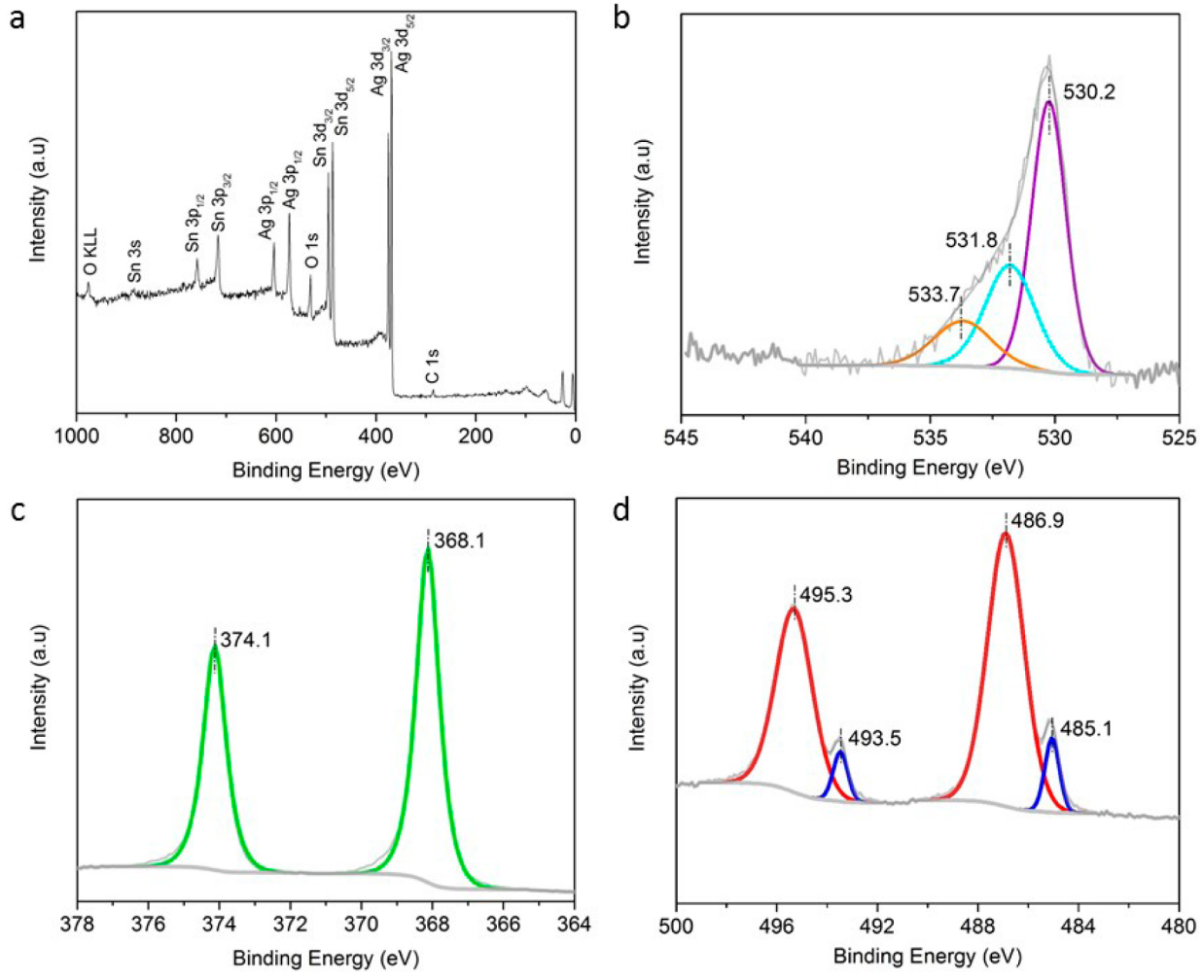

Figure 2. XPS spectra of $Ag_{76}Sn_{24}$: (a) overall survey spectrum, (b) O 1s spectrum, (c) Ag 3d spectrum, and (d) Sn 3d spectrum. Solid color lines represent the curve fittings.

DOI: 10.1021/jacs.6b10435
J. Am. Chem. Soc. 2017, 139, 1885–1893

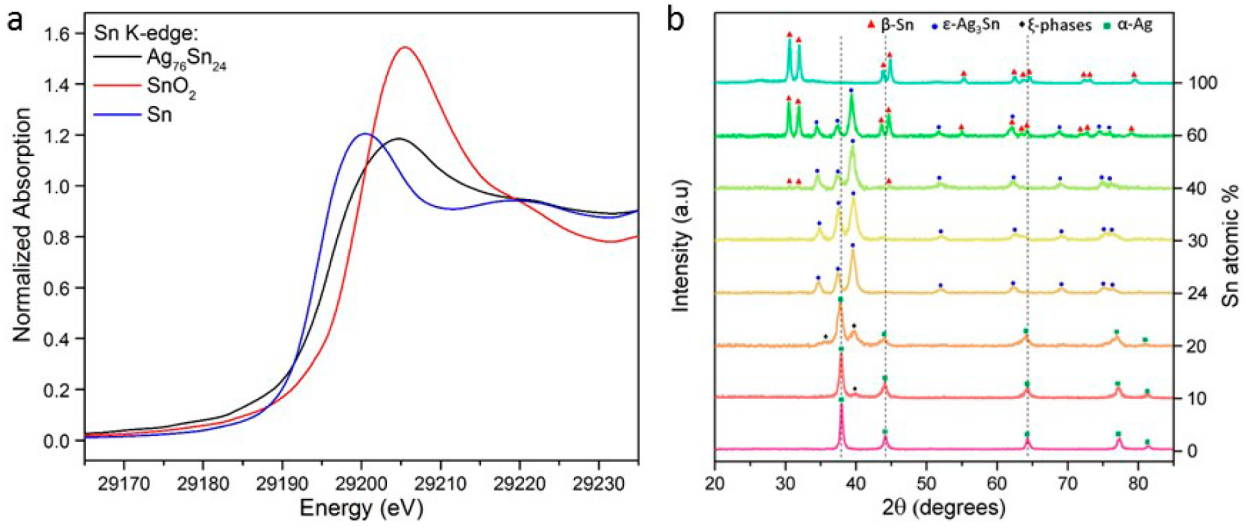

Figure 3. (a) X-ray absorption near-edge structure spectrum for $Ag_{76}Sn_{24}$. Spectra for SnO_2 and Sn standards were shown for comparison. (b) Powder X-ray diffraction patterns for AgSn/SnO_x catalysts.

obtained from XPS analysis agreed well with the bulk compositions. While the tin species on the catalyst surface was primarily partially oxidized SnO_x, metallic Sn was also detected and its percentage increased slightly at higher bulk Sn concentrations. The XPS results clearly proved that the amount of partially oxidized SnO_x presented on the catalyst surface correlated well with the bulk Sn concentration. The presence of PVP residue (less than 1.5 wt %) was observed using thermogravimetric analysis.

The presence of partially oxidized SnO_x in the $Ag_{76}Sn_{24}$ catalyst was further confirmed by X-ray absorption spectroscopy (XAS). The Sn K-edge X-ray absorption near-edge structure (XANES) spectra for $Ag_{76}Sn_{24}$ together with the standards are shown in Figure 3a. The spectrum for $Ag_{76}Sn_{24}$ shows a clear edge shift toward higher energy with respect to the edge of metallic Sn, indicating that the Sn atoms in $Ag_{76}Sn_{24}$ catalyst was, at least partially, oxidized. Additionally, the Sn K-edge of SnO_2 is at much higher energy than that of $Ag_{76}Sn_{24}$, confirming that the Sn atoms were not fully oxidized to its 4+ state. On the basis of both XPS and XANES results, the AgSn/SnO_x catalyst had a partially oxidized SnO_x surface layer with a metallic Ag−Sn core.

The atomic structures of the as-prepared catalysts were analyzed using powder X-ray diffraction (PXRD) and the diffraction patterns are shown in Figure 3b. There are four dominant crystal phases in the Ag−Sn binary system.[22] The pure Ag showed a face-centered cubic α-phase structure, while the catalysts with 10−20 atomic % Sn showed an additional disordered close-packed hexagonal ξ-phase. With 24 atomic % Sn, a pure orthorhombic ε-phase was obtained, which is associated with the intermetallic Ag_3Sn compound and is in good agreement with the HRTEM result (Figure 1c). At high Sn concentrations, the catalysts were a mixture of ε-phase and Sn-rich body-centered tetragonal β-Sn phase, with the β-Sn phase becoming more prevalent as the Sn concentration increased. Diffraction patterns with label facets are shown in Supplementary Figure S4. At all Ag/Sn compositions, no crystalline oxide phases were observed in the PXRD patterns, suggesting that the surface partially oxidized SnO_x layer was amorphous and is consistent with the observation shown in Figure 1c. The phase transitions along with the Sn concentrations in the Ag−Sn binary alloys are in good agreement with the Ag−Sn binary phase diagram (Supplementary Figure S5). The crystallite sizes of AgSn/SnO_x catalysts were estimated using the Scherrer formula and the average sizes were in the range of 10 to 20 nm (Supplementary Table S1).

Electrocatalytic Evaluation. The electrocatalytic CO_2 reduction performance of the as-synthesized AgSn/SnO_x catalysts were evaluated in a two-compartment batch cell using a typical three-electrode setup. A 0.5 M $NaHCO_3$ solution saturated with CO_2 (pH = 7.2) was used as the electrolyte. At the applied potential of −0.8 V vs reversible hydrogen electrode (RHE), the AgSn/SnO_x catalysts produced a significant amount of formate as the dominate CO_2 reduction product (Figure 4). The only observed CO_2 reduction products

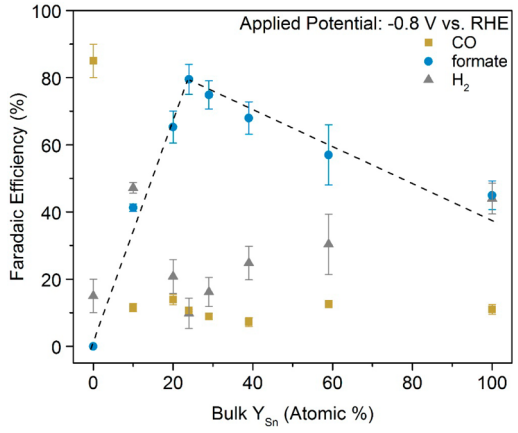

Figure 4. CO_2 reduction Faradaic efficiencies of AgSn/SnO_x catalysts.

were CO and formate and their Faradaic efficiencies were calculated from gas chromatograph and NMR spectroscopy quantification methods. The remaining charge balance was assumed to be attributed to the hydrogen evolution reaction. All reported potentials were corrected for internal resistance associated with the electrolyte. It is striking that a volcano-type correlation was observed between the Sn concentration in the AgSn/SnO_x catalysts and the formate Faradaic efficiency. When

DOI: 10.1021/jacs.6b10435
J. Am. Chem. Soc. 2017, 139, 1885−1893

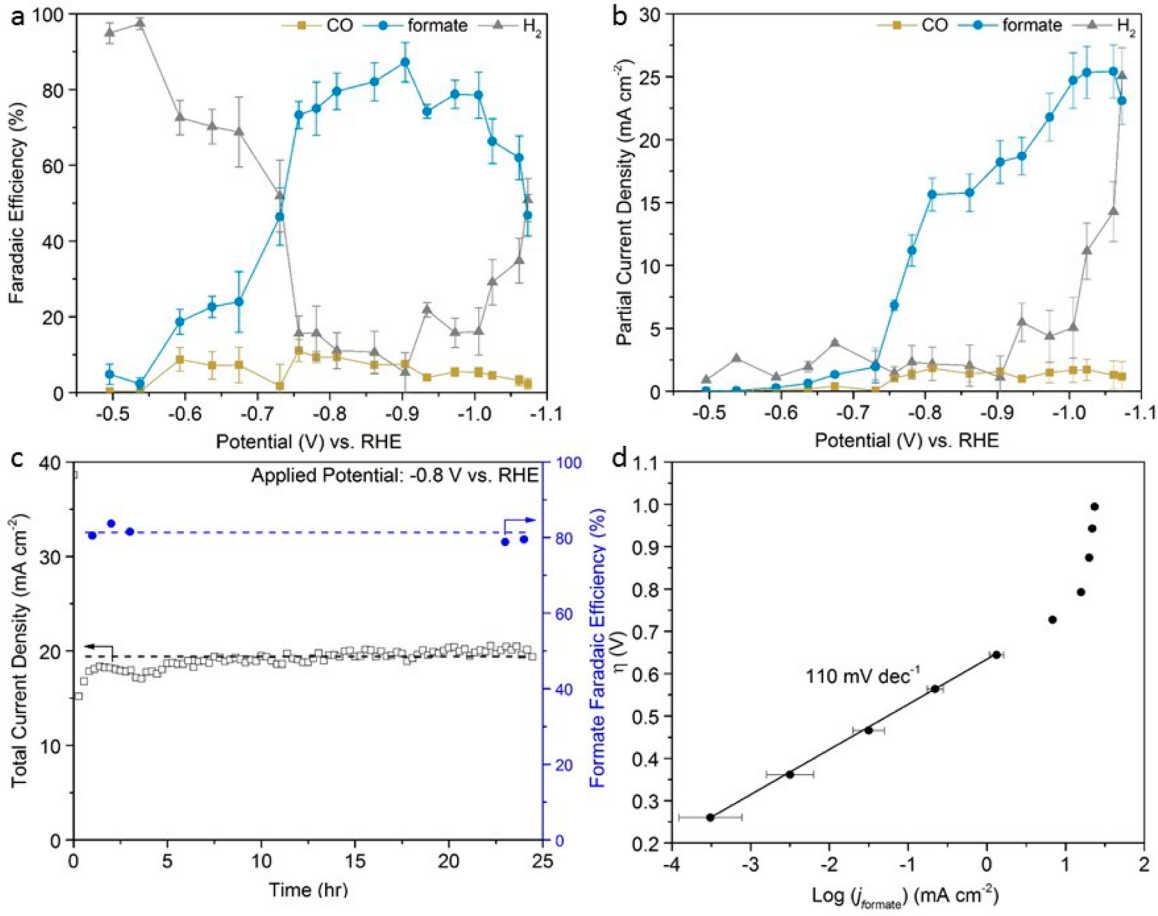

Figure 5. Electrochemical CO_2 reduction performance of $Ag_{76}Sn_{24}$ catalyst: (a) CO, formate, and H_2 Faradaic efficiencies, (b) CO, formate, and H_2 partial current densities, (c) long-term stability performance, and (d) Tafel analysis.

the catalyst surface is fully covered by the amorphous SnO_x layer, the expected formate Faradaic efficiency should level off; however, Figure 4 shows a significant decrease in formate Faradaic efficiency for Ag−Sn catalysts with high Sn concentrations. Since SnO_x is less conductive in comparison to metallic Sn or AgSn alloys, the high percentage of SnO_x on the surface (Supplementary Table S2, Figures S6a and S7a) likely compromises the electrical conductivity of the catalyst particles, resulting in lower formate Faradaic efficiencies.[18] At 24 atomic % of Sn content (i.e., $Ag_{76}Sn_{24}$), an optimal thickness (~1.7 nm) of SnO_x layer was achieved, and thus the highest formate Faradaic efficiency (~80%) was observed. Ideally, a similar catalyst composed of a ~1.7 nm thin layer of SnO_x, but instead with a pure Ag or Sn core should exhibit similar catalytic properties as the $AgSn/SnO_x$ catalyst with a Ag_3Sn core. However, for this work, the bimetallic core was tuned to control the amount of surface SnO_x. While the electrocatalysis data clearly showed the correlation between the amount of surface SnO_x and formate Faradaic efficiency, the catalyst surface under CO_2 electrolysis conditions are not necessarily the same as what we observed in the ex situ structural characterizations. As suggested by early works that showed a metastable SnO_x layer could be preserved under reducing potentials,[13,17,23] the partially oxidized SnO_x surface on the $AgSn/SnO_x$ catalysts was very likely preserved and responsible for the electrochemical reduction of CO_2 to formate.

Turning to the CO Faradaic efficiencies, the pure Ag catalyst was highly CO selective (Supplementary Figures S6b and S7b), while a slight introduction of Sn into the Ag−Sn alloy system dramatically suppressed the production of CO. There was no correlation between the bulk Ag atomic % on CO Faradaic efficiency (Figure 4) and this further suggests that the surface was primarily consisted of SnO_x and not Ag. During the synthesis of the $AgSn/SnO_x$ catalysts, the difference in surface energy between Sn and Ag caused Sn to spontaneously aggregate toward the surface to minimize the surface energy of the nanoparticle, which subsequently formed the SnO_x surface layer.[24,25] In addition, the formation of the SnO_x was suppressed if the surface was largely terminated by Ag; and thus, as the Ag composition increased, the amount of SnO_x decreased. This also indicates that the oxygen coverage on the particle surface is likely affected by the type of terminal atoms at the surface as reflected by the distribution of O specie in Figure 1g. Although PVP was detected by thermogravimetric analysis, the amount of surfactant was consistent across all samples; therefore, the presence of PVP had minimal effect on the CO_2 reduction trends in this work.

Since the $Ag_{76}Sn_{24}$ catalyst showed the most promising properties for electrochemical CO_2 reduction, the catalyst was further investigated under various applied potentials. Figure 5a shows the CO and formate Faradaic efficiencies as a function of potential, which describes the selectivity of CO_2 electroreduction. As the potential became more negative from −0.5 V to −0.9 V vs RHE, the formate Faradaic efficiency increased and reached a maximum of 87.2% at −9.0 V vs RHE. At more negative potentials the formate Faradaic efficiencies decreased.

DOI: 10.1021/jacs.6b10435
J. Am. Chem. Soc. 2017, 139, 1885−1893

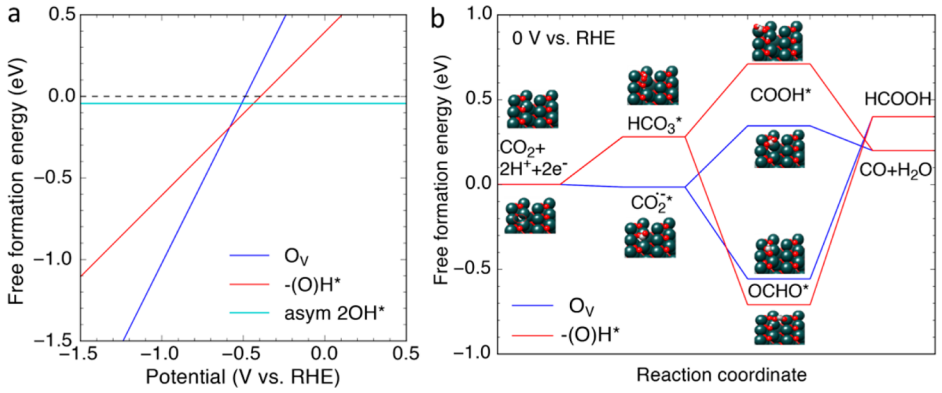

Figure 6. (a) The free formation energies of surface defects (O_v: oxygen vacancy, −(O)H*: hydroxyl from H^+ reduction, and asymmetric 2OH* from chemical water dissociation) on the SnO as a function of potentials vs RHE. (b) The most favorable free energy pathways of CO and HCOOH formation on SnO with O_v and −(O)H*, respectively.

On average, the CO faradaic efficiency was less than 10% and the remaining balance was attributed to the production of hydrogen by proton reduction. The formate partial current density (Figure 5b) reached a maximum of 25.4 mA cm^{-2} at −1.06 V vs RHE with a total current density of 26.7 mA cm^{-2} for the electroreduction of CO_2. At this potential of −1.06 V vs RHE, the catalyst's catalytic activity was 6.1 × 10^{-3} (g of formate)(g of catalysts)$^{-1}$(sec)$^{-1}$. The partial current density decreased at very negative potentials (<−1.06 V vs RHE), which was likely associated with CO_2 diffusion limitation. The long-term stability of the $Ag_{76}Sn_{24}$ catalyst was investigated using a batch-type two-compartment cell and a highly stable current in the span of 24 h was achieved, suggesting that the ultrathin partially oxidized SnO_x layer is stable for long-term operation under realistic conditions. The spent catalyst was characterized using XPS and only a slight reduction of SnO_x to metallic Sn was observed (Supplementary Figure S11), which further confirms the highly stable nature of the amorphous SnO_x layer. In comparison to other formate-selective electrocatalysts, the $Ag_{76}Sn_{24}$ catalyst is one of the best electrocatalysts for CO_2 reduction to formate in terms of overpotential, formate partial current density, and formate Faradaic efficiency as illustrated in the Supplementary Table S3, Figures S12 and S13.[9,13,14,18,20,26−29] As mentioned earlier, the partially oxidized cobalt catalyst exhibited a superior formate selectivity at low overpotentials;[20] however, the formate partial current density for this catalyst was limited to ∼8 mA cm^{-2}, which is much lower than the current density (∼25 mA cm^{-2}) of the $Ag_{76}Sn_{24}$ catalyst reported in this work.

To gain kinetic insights for CO_2 electroreduction to formate on the $Ag_{76}Sn_{24}$ catalyst, the formate partial current density at various overpotentials were measured and a Tafel plot was constructed (Figure 5d). A Tafel slope of 110 mV dec^{-1} was obtained for the $Ag_{76}Sn_{24}$ catalyst, which indicates that the rate-determining step was the first electron transfer step. The Tafel slope was similar to the slope (∼117 mV dec^{-1}) of Sn_{100} (Supplementary Figure S14), which is a partially oxidized Sn/SnO_x catalyst with a similar core−shell structure (Supplementary Figure S15). The slope is also consistent with other literature-reported values, although a slope of ∼70 mV $decade^{-1}$ was also reported for some Sn-based catalysts.[13,18,29] Because the Tafel slope is dependent on many factors, such as operating potentials, intermediate surface coverage, surface properties, and mass transfer effects, future mechanistic studies are required to determine the actual reaction mechanism on the partially oxidized SnO_x surface.

Computational Analysis. The computational modeling was performed to elucidate the origin of the superior CO_2 reduction activity of AgSn/SnO_x catalysts. The stability of different surface defects of the most stable SnO(101) was first studied under CO_2 electrochemical reduction conditions. The model system was based on the structural information obtained from STEM-EELS elemental mapping and XPS analysis (Figures 1 and 2), which showed a surface layer of partially oxidized tin (SnO_x). At reaction conditions (−0.8 V vs RHE), the surface tin oxide layer can be partially reduced to Sn^{2+} oxide, even though the Pourbaix diagram (Supplementary Figure S16) suggests that metallic Sn is thermodynamically stable at the highly negative potentials. Figure 6a shows the free formation energies of oxygen vacancy O_v, embedded hydroxyl −(O)H* from proton reduction, and asymmetric hydroxyls (noted as asym 2OH*) from chemical water dissociation relative to the stoichiometric surface as a function of electrode potential vs RHE (see the Supporting Information for additional details). The oxygen vacancy was stable at highly negative potentials (less than −0.6 V vs RHE) while the embedded hydroxyl was present at potentials between −0.6 V and −0.4 V. At potentials higher than −0.4 V, the formation of asymmetric hydroxyls through a chemical water splitting was thermodynamically favorable. Figure 6b shows the most favorable free energy pathways of CO_2 reduction toward formate and CO on a SnO surface with O_v and −(O)H* at 0 V vs RHE. CO_2 adsorption on the oxygen-vacant site is thermally neutral and a significant electron transfer was observed indicating the formation of adsorbed CO_2 negative ion. However, CO_2 adsorption on −(O)H* surface preferred the insertion pathway with +0.3 eV free energy barrier at 0 V vs RHE. The formation of OCHO* intermediate on both surfaces was highly favorable compared to the formation of COOH*. Assuming the activation barrier of the proton transfer reactions scales with the free energy driving force, the HCOOH formation pathway via the OCHO* intermediate is the selective pathway on both surfaces. The activity of asymmetric OH* is not shown here because it is only stable under high potentials.

To understand the general trend of catalytic performance at −0.8 V vs RHE due to variations in bulk composition of Ag−Sn core, the free formation energies of OCHO* and COOH* as a function of CO_2* adsorption energy on a series of expanded

DOI: 10.1021/jacs.6b10435
J. Am. Chem. Soc. 2017, 139, 1885−1893

SnO surfaces with oxygen vacancies were studied (Supplementary Figure S17). The free formation energies of OCHO* and COOH* were linearly correlated with that of adsorbed *CO_2 with the scaling factors 1.71 and 0.83, respectively.[30] Clearly, as the SnO surface expanded in response to the increased concentration of Sn in the Ag−Sn core, the free energy driving force for OCHO* increased due to further stabilization of OCHO* relative to CO_2*, thus rationalizing the enhanced reactivity toward HCOOH formation. Conversely, the formation energies of COOH* and CO_2* were affected by a similar extent; therefore, the free energy driving force for the CO formation pathway was not sensitive to the variation of the surface lattice, consistent with the experimental observations that CO Faradaic efficiency stayed almost the same as the Ag−Sn composition changed. At high Sn concentrations, a thick layer of the surface tin oxide was formed, thus lowering the current density due to the loss of electrical conductivity.

■ CONCLUSION

In summary, a core−shell electrocatalysts with a Ag−Sn bimetallic core and an ultrathin partially oxidized SnO_x shell was synthesized for high-performance CO_2 conversion to formate. Detailed structural characterizations including SEM, TEM, and XPS proved the successfully syntheses of the core−shell electrocatalysts as well as the successfully manipulation of the partially oxidized SnO_x shell. Furthermore, a structure−property correlation between the AgSn/SnO_x core−shell structure and CO_2 electrocatalytic property was established by studying a series of Ag−Sn catalysts with different Ag/Sn compositions. A volcano-like correlation between the bulk composition and electrocatalytic performance was observed, which suggested that the optimal thickness of the partially oxidized SnO_x shell is ∼1.7 nm. In addition, the electro-kinetic studies showed a Tafel slope of ∼110 mV decade^{-1} for CO_2 conversion to formate, which indicates that the rate-determining step was the first electron transfer step. With density-functional theory calculations on SnO (101) surface with oxygen vacancies, we showed that such a volcano-like relationship arises from the competing effects of favorable stabilization of the OCHO* intermediate by lattice expansion and the electrical conductivity loss due to the increased thickness of the SnO_x layer.

■ EXPERIMENTAL METHODS

Preparation of AgSn/SnO_x Core−Shell Nanoparticles. AgSn/SnO_x core−shell nanoparticles were synthesized using an adopted seed growth and galvanic displacement method.[21] For the synthesis of $Ag_{76}Sn_{24}$, 0.230 g of Tin(II) acetate ($Sn(Ac)_2$, Sigma-Aldrich) and 4.06 g of polyvinylpyrrolidone (PVP, M_W = 55,000, Sigma-Aldrich) were added to 100 mL of 1,5-pentanediol (96%, Sigma-Aldrich) in a 250 mL three-neck round flask. The solution was heated to 120 °C and stirred under inert atmosphere. Next, Sn nanoparticles were precipitated out by adding 1.382 g of sodium borohyride ($NaBH_4$, 99%, Sigma-Aldrich) into solution. After 10 min, a silver nitrate ($AgNO_3$, Sigma-Aldrich) solution made by dissolving 0.280 g of $AgNO_3$ was added into the mixture. This resulted in the galvanic displacement between metallic Sn and Ag^+ on the basis of reduction potentials. The solution was then heated to 180 °C while being stirred for 2 h. The resulting AgSn/SnO_x nanoparticles were centrifuged at 5500 rpm and washed with methanol and ethanol several times to remove surfactant and then dried in air at 60 °C. Other compositions of Ag−Sn bimetallic nanoparticles were synthesized by changing the quantities of the Ag and Sn starting materials. This synthetic procedure is robust and highly reproducible.

Structural Characterizations. The crystal structure of the as-synthesized nanoparticles was examined using powder X-ray diffraction (PXRD) on a Bruker D8 Discover diffractometer using a Cu Kα radiation source. The bulk composition was analyzed with a Rigaku wavelength dispersive X-ray fluorescence (WDXRF) spectrometer. Scanning electron microscopy (SEM) images were collected using a Zeiss Auriga-60. A JEOL JEM-2100F TEM equipped with HAADF-STEM detector and operated at an accelerating voltage of 200 kV was used for transmission electron microscopy (TEM), HRTEM, HAADF-STEM imaging and EELS analysis. To analyze the surface stoichiometry a Thermo Scientific K-Alpha X-ray Photoelectron Spectrometer (XPS) System was used. The XPS data were calibrated using the binding energy of adventitious carbon at 285 eV and analyzed using CasaXPS software. All peaks were fitted using a Gaussian/Lorentzian product line shape and a Shirley background.

Electrode Fabrication. Electrodes were prepared by making a suspension with a proportion of 50 mg of AgSn/SnO_x nanoparticles, 1.2 mL of DI water, 1.2 mL of isopropyl alcohol, and 20 μL of D521 5 wt % Nafion solution (DuPont). The suspension was sonicated to achieve a homogeneous dispersion. The resulting suspension was then uniformly coated onto a gas diffusion layer of Sigracet 25 BC until a catalyst loading of 1 mg cm^{-2} was achieved. At one end of the electrode, a nickel wire as the current collector was attached using silver paint (SPI Supplies). The apparent electrode size used was ∼0.5 cm^2.

Electrocatalysis Evaluation. A typical three-electrode gastight two-compartment setup was used to characterize the catalytic performance (Supplementary Figure S18). A piece of platinum wire was used as the counter electrode and an Ag/AgCl (3.0 M KCl, BASi) electrode was used as the reference electrode. The reference potentials were converted to RHE using the formulas E(RHE) = E(Ag/AgCl) + 0.210 V + 0.0591 M × pH. The electrolyte was 0.5 M bicarbonate ($NaHCO_3$) solution which was prepared by dissolving sodium carbonate ($NaCO_3$, ≥99.999%, Fluka) in DI water and purging the solution with CO_2 gas (99.9999%, Keen Gas). The final electrolyte was 0.5 M $NaHCO_3$ saturated with CO_2 (pH = 7.2). A cation exchange membrane (Nafion 115) was used as the compartment separator. Each compartment contained 40 mL of electrolyte with a ∼50 mL headspace. Before electrolysis, the electrolyte was purged with CO_2 gas for at least 15 min and the headspace at least 20 min. The electrolyte in the cathodic compartment was stirred at a rate of 1200 rpm. The quantification of gaseous CO_2 reduction products was conducted using a gas chromatograph (SHIMADZU, GC-2014) equipped with a PLOT MolSieve 5A column and a Q-bond PLOT column. Gas-phase products were sampled every 30 min using a gastight syringe (Hamilton). Liquid products were quantified using a Bruker AVIII 600 MHz NMR spectrometer. Typically, 500 μL of electrolyte was sampled at the conclusion of the electrolysis was mixed with 100 μL D_2O, and 1.67 ppm (m/m) dimethyl sulfoxide (≥99.9%, Alfa Aesar) was added as the internal standard. The one-dimensional ^{1}H spectrum was measured with water suppression using a presaturation method.

A Princeton Applied Research VersaSTAT 3 potentiostat was used for all CO_2 reduction experiments. Constant potential electrolysis was used to measure the catalytic performance of the Ag−Sn electrodes. For a typical experiment, pre-electrolysis was conducted at constant potential of −1.1 vs RHE for at least 10 min. Immediately, the electrode was then washed with DI water and placed into another electrochemical cell. The electrolyte and head space were purged with CO_2 and then electrochemical cell was sealed airtight and set at the desired potential for a 1 h electrolysis experiment. Internal resistance of the solution was measured after electrolysis using a Solartron SI 1287 potentiostat and the reported applied potential was adjusted accordingly. Typically, small resistances ranging from 8 to 10 Ω were measured. Electrochemical results were obtained across several replicate measurements with separately prepared electrodes. As for the 24h durability test, the headspace was continuously purge with CO_2 at 10 mL min^{-1} during electrolysis. Small quantity of electrolyte samples were taken at the first 3 h of the electrolysis experiment to determine initial formate Faradaic efficiencies and then the electrolysis

DOI: 10.1021/jacs.6b10435
J. Am. Chem. Soc. 2017, 139, 1885−1893

was allowed to proceed for 19 h without disturbance. Finally, electrolyte samples were taken for the last 2 h to determine the final formate Faradaic efficiencies to study the overall stability of the catalysts after 24 h of operation.

Computational Modeling. All electronic structure calculations were performed using the QUICKSTEP code provided by the CP2K package. The exchange-correlation potential was treated with the generalized gradient approximation parametrized by the spin-polarized Perdew–Burke–Ernzerhof functional (PBE).[31] The wave functions were expanded in an optimized double-ζ Gaussian basis sets (DZVP-MOLOPT-GTH) with an auxiliary plane-wave basis set with a cutoff energy of 480 Ry.[32,33] Brillouin zone integration was performed with a reciprocal space mesh consisting of only the gamma point. The DFT-D3 van der Waals correction by Grimme was applied to capture interactions between Sn–O–Sn stacking layer.[34] Core electrons was modeled by the scalar relativistic norm-conserving Goedecker–Teter–Hutter (GTH) potentials with 4, 6, 1, and 4 valence electrons for Sn, O, H and C, respectively. The Brillouin zone integration were performed with a reciprocal space mesh consisting of only the Gamma point. The SnO(101) surface with 4 layers and 2 × 3 unit cells containing 48 Sn atoms was used as the model system.[35] Tin monoxide has a tetragonal structure of space group 129 represented by the *P4/nmm* symmetry. The calculated lattice constant with a = 3.895 and c = 4.91 was close to experimental measurements with a = 3.8 and c = 4.83, In the cell and geometry optimizations, the maximum forces were converged to 0.025 eV/Å. Free formation energy of intermediates was calculated by considering the zero point energy, entropy, and solvation effect.[36] The DFT PBE functional error for gas phase CO and HCOOH was corrected using the experimental formation energy of CO and HCOOH.

■ ASSOCIATED CONTENT

Supporting Information

The Supporting Information is available free of charge on the ACS Publications website at DOI: 10.1021/jacs.6b10435.

Compositions and particle sizes of catalysts; additional structural characterization data; phase diagram; additional electrochemical data; comparison with literature data; Pourbaix diagram of tin; additional computational information; reactor setup (PDF)

■ AUTHOR INFORMATION

Corresponding Author

*jiao@udel.edu

ORCID

Siwen Wang: 0000-0003-3582-5398

Feng Jiao: 0000-0002-3335-3203

Notes

The authors declare no competing financial interest.

■ ACKNOWLEDGMENTS

The authors at University of Delaware would like to thank the National Science Foundation Faculty Early Career Development (CAREER) program (Award No. CBET-1350911) for financial support. The authors at Virginia Polytechnic Institute and State University acknowledge the support from American Chemical Society Petroleum Research Fund (ACS PRF) and NSF CBET Catalysis and Biocatalysis Program (CBET-1604984). The electron microscopy work made use of the EPIC facility of the NUANCE Center at Northwestern University, which has received support from the Soft and Hybrid Nanotechnology Experimental (SHyNE) Resource (NSF NNCI-1542205); the MRSEC program (NSF DMR-1121262) at the Materials Research Center; the International Institute for Nanotechnology (IIN); the Keck Foundation; and the State of Illinois, through the IIN. This research used resources of the Advanced Photon Source, a U.S. Department of Energy (DOE) Office of Science User Facility operated for the DOE Office of Science by Argonne National Laboratory under Contract No. DE-AC02-06CH11357.

■ REFERENCES

(1) Asadi, M.; Kumar, B.; Behranginia, A.; Rosen, B. A.; Baskin, A.; Repnin, N.; Pisasale, D.; Phillips, P.; Zhu, W.; Haasch, R.; Klie, R. F.; Kral, P.; Abiade, J.; Salehi-Khojin, A. *Nat. Commun.* **2014**, *5*, 4470.

(2) Choi, J.; Kim, M. J.; Ahn, S. H.; Choi, I.; Jang, J. H.; Ham, Y. S.; Kim, J. J.; Kim, S. K. *Chem. Eng. J.* **2016**, *299*, 37–44.

(3) Lu, Q.; Rosen, J.; Jiao, F. *ChemCatChem* **2015**, *7* (1), 38–47.

(4) Manthiram, K.; Beberwyck, B. J.; Aivisatos, A. P. *J. Am. Chem. Soc.* **2014**, *136* (38), 13319–13325.

(5) Monzo, J.; Malewski, Y.; Kortlever, R.; Vidal-Iglesias, F. J.; Solla-Gullon, J.; Koper, M. T. M.; Rodriguez, P. *J. Mater. Chem. A* **2015**, *3* (47), 23690–23698.

(6) Rasul, S.; Anjum, D. H.; Jedidi, A.; Minenkov, Y.; Cavallo, L.; Takanabe, K. *Angew. Chem., Int. Ed.* **2015**, *54* (7), 2146–2150.

(7) Sen, S.; Liu, D.; Palmore, G. T. R. *ACS Catal.* **2014**, *4* (9), 3091–3095.

(8) Chen, Y.; Li, C. W.; Kanan, M. W. *J. Am. Chem. Soc.* **2012**, *134* (49), 19969–72.

(9) Hori, Y.; Wakebe, H.; Tsukamoto, T.; Koga, O. *Electrochim. Acta* **1994**, *39* (11–12), 1833–1839.

(10) Lu, Q.; Rosen, J.; Zhou, Y.; Hutchings, G. S.; Kimmel, Y. C.; Chen, J. G.; Jiao, F. *Nat. Commun.* **2014**, *5*, 3242.

(11) Zhu, W. L.; Michalsky, R.; Metin, O.; Lv, H. F.; Guo, S. J.; Wright, C. J.; Sun, X. L.; Peterson, A. A.; Sun, S. H. *J. Am. Chem. Soc.* **2013**, *135* (45), 16833–16836.

(12) Zhu, W. L.; Zhang, Y. J.; Zhang, H. Y.; Lv, H. F.; Li, Q.; Michalsky, R.; Peterson, A. A.; Sun, S. H. *J. Am. Chem. Soc.* **2014**, *136* (46), 16132–16135.

(13) Chen, Y. H.; Kanan, M. W. *J. Am. Chem. Soc.* **2012**, *134* (4), 1986–1989.

(14) Choi, S. Y.; Jeong, S. K.; Kim, H. J.; Baek, I.-H.; Park, K. T. *ACS Sustainable Chem. Eng.* **2016**, *4* (3), 1311–1318.

(15) Kumar, B.; Llorente, M.; Froehlich, J.; Dang, T.; Sathrum, A.; Kubiak, C. P. *Annu. Rev. Phys. Chem.* **2012**, *63*, 541.

(16) Rosen, J.; Hutchings, G. S.; Lu, Q.; Forest, R. V.; Moore, A.; Jiao, F. *ACS Catal.* **2015**, *5* (8), 4586–4591.

(17) Zhang, R.; Lv, W. X.; Lei, L. X. *Appl. Surf. Sci.* **2015**, *356*, 24–29.

(18) Zhang, S.; Kang, P.; Meyer, T. J. *J. Am. Chem. Soc.* **2014**, *136* (5), 1734–1737.

(19) Lu, Q.; Jiao, F. *Nano Energy* **2016**, *29*, 439.

(20) Gao, S.; Lin, Y.; Jiao, X.; Sun, Y.; Luo, Q.; Zhang, W.; Li, D.; Yang, J.; Xie, Y. *Nature* **2016**, *529* (7584), 68–71.

(21) Jo, Y. H.; Jung, I.; Kim, N. R.; Lee, H. M. *J. Nanopart. Res.* **2012**, *14* (4), 782–791.

(22) Karakaya, I.; Thompson, W. T. *Bull. Alloy Phase Diagrams* **1987**, *8*, 349.

(23) Baruch, M. F.; Pander, J. E.; White, J. L.; Bocarsly, A. B. *ACS Catal.* **2015**, *5* (5), 3148–3156.

(24) Tyson, W. R.; Miller, W. A. *Surf. Sci.* **1977**, *62* (1), 267–276.

(25) Vitos, L.; Ruban, A. V.; Skriver, H. L.; Kollar, J. *Surf. Sci.* **1998**, *411* (1–2), 186–202.

(26) Lei, F. C.; Liu, W.; Sun, Y. F.; Xu, J. Q.; Liu, K. T.; Liang, L.; Yao, T.; Pan, B. C.; Wei, S. Q.; Xie, Y. *Nat. Commun.* **2016**, *7*, 12697.

(27) Wang, H.; Chen, Y.; Hou, X.; Ma, C.; Tan, T. *Green Chem.* **2016**, *18* (11), 3250–3256.

(28) Watanabe, M.; Shibata, M.; Kato, A.; Azuma, M.; Sakata, T. *J. Electrochem. Soc.* **1991**, *138* (11), 3382–3389.

(29) Won, D. H.; Choi, C. H.; Chung, J.; Chung, M. W.; Kim, E. H.; Woo, S. I. *ChemSusChem* **2015**, *8* (18), 3092–3098.

DOI: 10.1021/jacs.6b10435
J. Am. Chem. Soc. 2017, 139, 1885–1893

(30) Abild-Pedersen, F.; Greeley, J.; Studt, F.; Rossmeisl, J.; Munter, T. R.; Moses, P. G.; Skulason, E.; Bligaard, T.; Norskov, J. K. *Phys. Rev. Lett.* **2007**, *99* (1), 016105.
(31) Perdew, J. P.; Burke, K.; Ernzerhof, M. *Phys. Rev. Lett.* **1996**, *77* (18), 3865−3868.
(32) VandeVondele, J.; Hutter, J. *J. Chem. Phys.* **2007**, *127* (11), 114105.
(33) VandeVondele, J.; Krack, M.; Mohamed, F.; Parrinello, M.; Chassaing, T.; Hutter, J. *Comput. Phys. Commun.* **2005**, *167* (2), 103−128.
(34) Grimme, S.; Antony, J.; Ehrlich, S.; Krieg, H. *J. Chem. Phys.* **2010**, *132* (15), 154104.
(35) Pang, C. L.; Haycock, S. A.; Raza, H.; Moller, P. J.; Thornton, G. *Phys. Rev. B: Condens. Matter Mater. Phys.* **2000**, *62* (12), R7775−R7778.
(36) Karamad, M.; Hansen, H. A.; Rossmeisl, J.; Norskov, J. K. *ACS Catal.* **2015**, *5* (7), 4075−4081.

DOI: 10.1021/jacs.6b10435
J. Am. Chem. Soc. 2017, 139, 1885−1893